

## RESEARCH LETTER

10.1002/2014GL061644

## Key Points:

- Three-dimensional spectral-element and frequency-wave number (SEM-FK) hybrid methods
- Accurate modeling of teleseismic converted and scattered waves
- High-resolution teleseismic array analysis

## Correspondence to:

P. Tong,  
tongping85@gmail.com

## Citation:

Tong, P., D. Komatitsch, T.-L. Tseng, S.-H. Hung, C.-W. Chen, P. Basini, and Q. Liu (2014), A 3-D spectral-element and frequency-wave number hybrid method for high-resolution seismic array imaging, *Geophys. Res. Lett.*, 41, 7025–7034, doi:10.1002/2014GL061644.

Received 29 AUG 2014

Accepted 8 OCT 2014

Accepted article online 12 OCT 2014

Published online 30 OCT 2014

## A 3-D spectral-element and frequency-wave number hybrid method for high-resolution seismic array imaging

Ping Tong<sup>1</sup>, Dimitri Komatitsch<sup>2</sup>, Tai-Lin Tseng<sup>3</sup>, Shu-Huei Hung<sup>3</sup>, Chin-Wu Chen<sup>4</sup>, Piero Basini<sup>1</sup>, and Qinya Liu<sup>1</sup>
<sup>1</sup>Department of Physics, University of Toronto, Toronto, Ontario, Canada, <sup>2</sup>LMA, CNRS UPR 7051, Aix-Marseille University, Centrale Marseille, Marseille, France, <sup>3</sup>Department of Geosciences, National Taiwan University, Taipei, Taiwan, <sup>4</sup>Institute of Oceanography, National Taiwan University, Taipei, Taiwan

**Abstract** We present a three-dimensional (3-D) hybrid method that interfaces the spectral-element method (SEM) with the frequency-wave number (FK) technique to model the propagation of teleseismic plane waves beneath seismic arrays. The accuracy of the resulting 3-D SEM-FK hybrid method is benchmarked against semianalytical FK solutions for 1-D models. The accuracy of 2.5-D modeling based on 2-D SEM-FK hybrid method is also investigated through comparisons to this 3-D hybrid method. Synthetic examples for structural models of the Alaska subduction zone and the central Tibet crust show that this method is capable of accurately capturing interactions between incident plane waves and local heterogeneities. This hybrid method presents an essential tool for the receiver function and scattering imaging community to verify and further improve their techniques. These numerical examples also show the promising future of the 3-D SEM-FK hybrid method in high-resolution regional seismic imaging based on waveform inversions of converted/scattered waves recorded by seismic array.

## 1. Introduction

Teleseismic array imaging based on converted and scattered waves is one of the essential tools for investigating the crustal and upper mantle structures, and has contributed significantly over the past three decades to our understanding of tectonic evolution and internal geodynamic processes [e.g., Rondenay, 2009; Kind et al., 2012; Liu and Gu, 2012]. Various methods including receiver function (RF) analysis through single station stacking [e.g., Langston, 1977; Yan and Clayton, 2007], common conversion point (CCP) stacking [e.g., Revenaugh, 1995; Sheehan et al., 2000; Chen et al., 2005], inverse scattering approaches based on asymptotic methods such as generalized Radon transform [e.g., Bostock et al., 2001; Cao et al., 2010; Shang et al., 2014], teleseismic migration [e.g., Shragge et al., 2006; Shang et al., 2012], and teleseismic scattering tomography [e.g., Frederiksen and Revenaugh, 2004; Pageot et al., 2013; Burdick et al., 2014; Tong et al., 2014] have been developed for specific imaging purposes.

RF analysis is a routine tool to characterize major discontinuities of the Earth's subsurface such as the Moho, 410 km and 660 km discontinuities [e.g., Rondenay, 2009; Kind et al., 2012]. However, restricted by its assumption on 1-D horizontally layered background model, RF analysis may have difficulty imaging geologically complex structures. Inverse scattering and migration techniques make less strong or no assumptions on the geometry and properties of subsurface structures but may require closely spaced stations to avoid spatial aliasing [e.g., Frederiksen and Revenaugh, 2004; Rondenay, 2009; Shang et al., 2012].

In recent years, the advent of new forward modeling techniques and increasing high-performance computing capacity make it feasible to numerically simulate the propagation of short-period teleseismic waves through regional heterogeneous models [e.g., Roecker et al., 2010; Monteiller et al., 2013; Tong et al., 2014]. These remarkable developments enable us to explore short-wavelength structures of the seismic array-side lithosphere at high resolution based on adjoint tomography [e.g., Tromp et al., 2005, 2008; Tape et al., 2009], a tomographic method that takes advantages of full 2-D/3-D numerical simulations in forward modeling and sensitivity kernel calculation, and iteratively refines velocity models and topography of interfaces through nonlinear optimization techniques [Liu and Gu, 2012; Tong et al., 2014]. Meanwhile, as the worldwide deployment of dense broadband seismic networks and arrays continues, both subsurface interfaces and volumetric material properties beneath seismic arrays may be expected to be resolved at

unprecedented resolution based on converted or scattered teleseismic waves [e.g., *Rondenay, 2009; Shang et al., 2012; Pageot et al., 2013*], especially in the framework of adjoint tomography [*Tong et al., 2014*].

Obtaining better estimates of the incident and scattered wavefields is a crucial step for teleseismic array analysis [*Rondenay, 2009*]. The spectral-element method (SEM) [e.g., *Komatitsch and Tromp, 1999; Tromp et al., 2008*] is the state-of-the-art technique that numerically solves the seismic wave equation and accurately simulates the propagation of seismic waves in geologically complex models. However, given standard computing cluster access, numerical simulations of seismic waves accurate to 8 s and lower at the global scale are still computationally expensive [e.g., *Tromp et al., 2008; Komatitsch et al., 2010*], not to mention the frequencies relevant to regional high-resolution imaging (e.g., 1–2 s for *P* waves and 3–6 s for *S* waves as in RF and scattering imaging studies) [e.g., *Liu and Gu, 2012; Monteiller et al., 2013*]. To reduce the amount of computation involved, the modeling of interactions of teleseismic waves and local structures can be achieved by hybrid methods that interface localized 2-D/3-D numerical solvers with fast-computed 1-D analytical solutions on the boundary [e.g., *Bielak and Christiano, 1984; Capdeville et al., 2003a, 2003b; Roecker et al., 2010; Monteiller et al., 2013*]. These hybrid methods assume simple 1-D background models outside of the domain of numerical simulations and that only 2-D/3-D effects inside the detailed computational domain contribute to the coda waves of teleseismic phases. As 2-D/3-D effects outside the domain are negligible, only incident wavefield for 1-D background models is needed for the boundary, which is very often true for stations at teleseismic distances [*Rondenay et al., 2008*].

In the proof-of-concept study of teleseismic array imaging based on adjoint tomography, *Tong et al. [2014]* developed a 2-D SEM-FK hybrid method that interfaces a frequency-wave number (FK) calculation, which provides semianalytical solutions to 1-D layered background models, with a 2-D SEM numerical solver to compute synthetic responses of local media to plane wave incidence. This 2-D SEM-FK hybrid method accurately deals with local heterogeneities and discontinuity undulations, and can be used as an efficient tool for the forward modeling of teleseismic converted and scattered waves. To implement teleseismic array imaging based on adjoint tomography further for realistic seismic data, in this study, we present a 3-D SEM-FK hybrid method and explore its ability in simulating teleseismic wave propagation in various local models.

## 2. Methodology

The propagation of teleseismic body waves as plane waves satisfies the homogeneous elastodynamics equation [*Aki and Richards, 2002*]

$$\rho(\mathbf{x}) \frac{\partial^2 \mathbf{u}(\mathbf{x}, t)}{\partial t^2} = \nabla \cdot \mathbf{T}(\mathbf{x}, t), \quad (1)$$

where  $\mathbf{u}$  is the displacement vector,  $\mathbf{T}$  is the stress tensor related to  $\mathbf{u}$  as  $\mathbf{T} = \lambda \nabla \cdot \mathbf{u} + \mu [\nabla \mathbf{u} + (\nabla \mathbf{u})^T]$  for isotropic Earth models considered in this study ( $T$  denotes the matrix transpose operator), and  $\rho$ ,  $\lambda$ , and  $\mu$  define the spatial distribution of density and Lamé elasticity parameters.

The displacement of an incident plane wavefield is determined by its incident angle  $\theta$  between the propagation direction and vertical  $\hat{\mathbf{z}}$ , as well as its horizontal traveling direction  $\hat{\mathbf{r}} = \hat{\mathbf{x}} \cos \phi + \hat{\mathbf{y}} \sin \phi$ , where  $\phi$  is the azimuth angle of  $\hat{\mathbf{r}}$  with respect to  $\hat{\mathbf{x}}$  (Figure 1a). In the local  $\hat{\mathbf{r}}\text{--}\hat{\mathbf{t}}\text{--}\hat{\mathbf{z}}$  Cartesian coordinate system, the displacement  $\mathbf{u} = (u_r, u_t, u_z)$  and the stress tensor  $\mathbf{T} = (T_{rr}, T_{rt}, T_{rz}, T_{tt}, T_{tz}, T_{zz})$  at any point within a stack of  $n$  layers responding to incident *P*, *SV*, and *SH* plane waves with incidence angle  $\theta$  from the half-space below can be analytically calculated by adapting the Thompson-Haskell propagator matrix technique, i.e., the frequency-wave number (FK) method (e.g., *Thomson [1950], Haskell [1953], Takeuchi and Saito [1972], Zhu and Rivera [2002]*, refer to *Tong et al. [2014]* for more details). Given the response of a 1-D layered medium to plane wave incidence in the 2-D plane of  $\hat{\mathbf{r}}\text{--}\hat{\mathbf{z}}$  outlined in *Tong et al. [2014]*, one can obtain the displacement and the stress responses in the  $\hat{\mathbf{x}}\text{--}\hat{\mathbf{y}}\text{--}\hat{\mathbf{z}}$  system through a simple coordinate transformation

$$\begin{aligned} u_x &= u_r \cos \phi - u_t \sin \phi, \\ u_y &= u_r \sin \phi + u_t \cos \phi; \\ T_{xx} &= T_{rr} \cos^2 \phi - T_{rt} \sin 2\phi + T_{tt} \sin^2 \phi, \\ T_{yy} &= T_{rr} \sin^2 \phi + T_{rt} \sin 2\phi + T_{tt} \cos^2 \phi, \end{aligned}$$

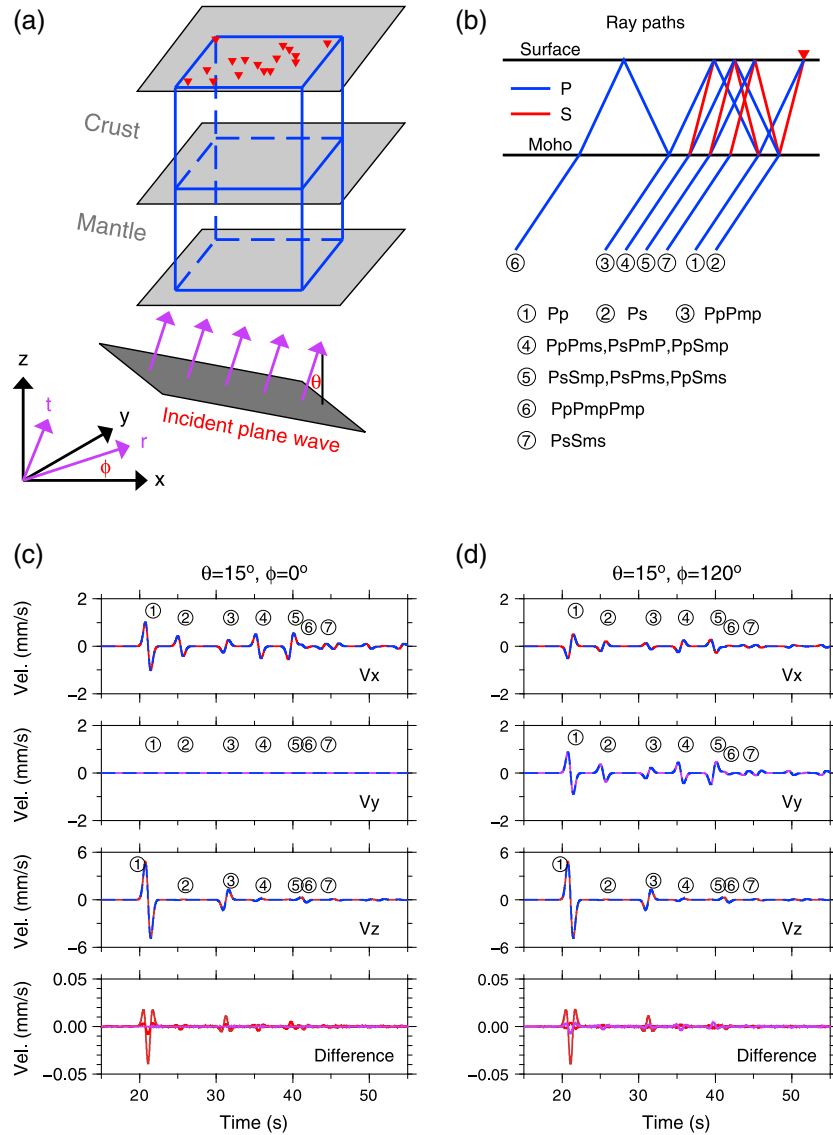


**Figure 1.** (a) Schematic illustration of the geometry for 3-D SEM-FK hybrid method. Purple arrows indicate the propagation direction of incident teleseismic plane waves (with incidence angle  $\theta$  with respect to vertical and azimuth angle  $\phi$  with respect to x axis). The region within the blue frame, i.e., the computational domain, is the local region of interest beneath the seismic array, encompassing all potential structural anomalies. It has the size of  $100 \text{ km} \times 60 \text{ km} \times 60 \text{ km}$ , and the Moho is at the depth of 30 km. Inverted triangles represent seismic stations located at the surface. (b) Raypaths of various phases generated by a plane P wave incidence into a crust-mantle model shown in Figure 1a, with blue and red line segments indicating the P and S legs, respectively. (c and d) The top three panels show the three-component velocity seismograms computed based on the FK (blue traces) and 3-D SEM-FK hybrid (dashed red traces) methods for a receiver at the right center of the surface. The bottom panel shows the difference between the FK and SEM-FK seismograms for the x (red), y (purple), and z (brown) components. The incidence angle of the plane waves is  $15^\circ$ , but the azimuth angles are  $0^\circ$  (Figure 1c) and  $120^\circ$  (Figure 1d), respectively. Various phases are labeled, and their corresponding raypaths are illustrated in Figure 1b. The size of each mesh element for the SEM calculation is 2.0 km.

$$\begin{aligned} T_{xy} &= (T_{rr} - T_{tt}) \sin \phi \cos \phi + T_{rt} \cos 2\phi, \\ T_{xz} &= T_{rz} \cos \phi - T_{tz} \sin \phi, \\ T_{yz} &= T_{rz} \sin \phi + T_{tz} \cos \phi. \end{aligned} \quad (2)$$

To model responses of heterogeneities in the array-side crust and upper mantle to teleseismic body wave incidence, we assume that the targeted heterogeneous region is embedded in a 1-D layered background model (Figure 1a) and encompassed by the simulation domain (indicated by the large blue box in Figure 1a).

**Table 1.** Material Properties for the One-Layer-Over-Half-Space (e.g., Crust-Mantle) Model in Figure 1a

	Density $\rho$ (kg/m <sup>3</sup> )	$V_p$ (m/s)	$V_s$ (m/s)
Crust	2600	5800	3198
Mantle	3380	8080	4485

spectral-element method naturally incorporate local heterogeneities and honor discontinuity undulations, and is one of the most accurate numerical techniques for seismic wave simulations [e.g., Komatitsch and Tromp, 1999; Komatitsch et al., 2004; Tromp et al., 2008]. The transition of plane wave propagation from 1-D background model into 3-D heterogeneous model can be implemented by imposing traction and velocity conditions on the boundaries, and the diffracted wavefield can be absorbed based on a simple and approximate absorbing condition of the Clayton and Engquist [1977] type, as mentioned in Monteiller et al. [2013] and Tong et al. [2014]

$$(\mathbf{T}_{\text{total}} - \mathbf{T}_{\text{FK}}) \cdot \hat{\mathbf{n}} = -\rho\alpha[\hat{\mathbf{n}} \cdot \partial_s(\mathbf{u}_{\text{total}} - \mathbf{u}_{\text{FK}})]\hat{\mathbf{n}} - \rho\beta[\hat{\mathbf{s}} \cdot \partial_s(\mathbf{u}_{\text{total}} - \mathbf{u}_{\text{FK}})]\hat{\mathbf{s}}, \quad (3)$$

where  $\hat{\mathbf{n}}$  is the unit outward normal of the boundary, and  $\hat{\mathbf{s}}$  is the unit vector tangential to the boundary [e.g., Komatitsch and Tromp, 1999]. Additionally, to accurately interface the FK and SEM calculation on the boundary, the boundary region of the 3-D SEM domain is required to smoothly transit from the 1-D layered background model to the 3-D heterogeneous structures. The resulting 3-D SEM-FK hybrid method can accurately handle local heterogeneities and discontinuity undulations, and represents an efficient tool for the modeling of teleseismic coda (including converted and scattered) waves beneath receiver arrays at frequencies relevant to scattering imaging [Tong et al., 2014].

### 3. Numerical Examples

#### 3.1. Benchmark for 1-D Models

We first benchmark the accuracy of the 3-D SEM-FK hybrid method against FK solutions for a 1-D crust-mantle model (Figure 1a, material properties listed in Table 1). Two plane  $P$  waves with the same incidence angle  $\theta = 15^\circ$  but different azimuth angles  $\phi = 0^\circ$  and  $\phi = 120^\circ$  are considered and assumed to follow a simple Gaussian source-time function (which remains the same for all other examples throughout this article) with a cut-off frequency  $f_0 = 2$  Hz:

$$f(t) = \frac{f_0}{\sqrt{\pi}} \exp[-(f_0 t)^2]. \quad (4)$$

Due to the presence of major discontinuities such as the Moho and the free surface, multiple secondary phases are generated as converted/reflected waves after the main  $P$  arrival (i.e.,  $P$  coda waves) at seismic arrays on the surface. The raypaths of the primary and various coda phases are shown in Figure 1b, and the three-component velocity seismograms recorded by a station deployed on the surface are shown in Figures 1c and 1d. The results of the 3-D SEM-FK hybrid method clearly match very well with those of the FK method, with a maximum difference less than 0.6% of the maximum amplitude of the velocity seismograms (Figures 1c and 1d). Meanwhile, the simulation only takes about 250 s to propagate the incidence plane waves for a duration of 160 s when 256 processor cores are used on a typical current computing cluster.

#### 3.2. Two-Layer Subducted Slab Model

To investigate the capability of our 3-D SEM-FK hybrid method in mapping realistic heterogeneous structures, we explore the interactions of obliquely incident plane  $P$  waves with a simplified 2-D subduction zone model that includes both fast and slow anomalies in the subducted slab as well as an undulated Moho (Figure 2a and Table 1), inspired by the Alaska subduction zone model imaged by Rondenay et al. [2008] based on the generalized Radon transform technique.

A plane  $P$  wave with a cut-off frequency  $f_0 = 0.5$  Hz, incidence angle  $\theta = 15^\circ$ , and azimuth angle  $\phi = 45^\circ$  is propagated into this subduction zone model by the 3-D SEM-FK hybrid method. For comparison, we also compute its propagation into a similar 2-D model with only undulated Moho and no slab anomalies (Figure 2b), as well as a 1-D crust over mantle model (Figure 2c). We calculate the radial, transverse,

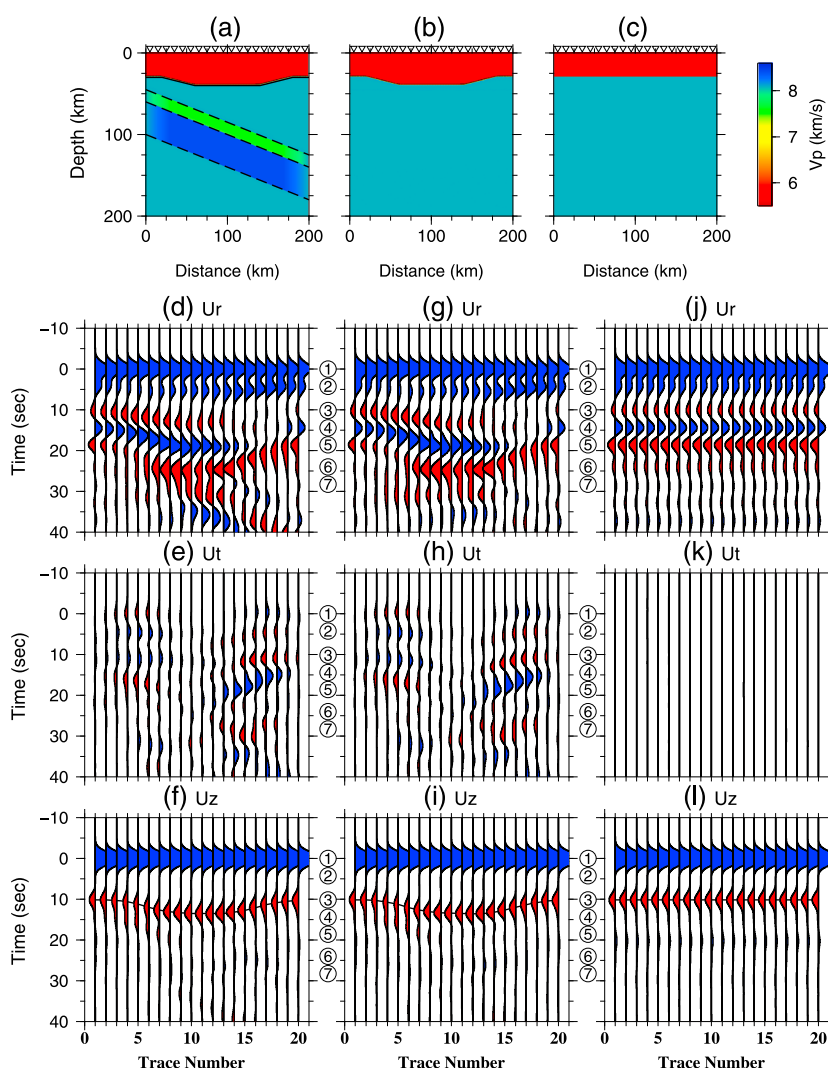


**Figure 2.** (a–c) Vertical views along the  $x$  axis of three different 2.5-D models, which are invariant along the  $y$  axis and have the same dimension of  $200 \text{ km} \times 200 \text{ km} \times 200 \text{ km}$ . Figure 2a resembles the Alaska subduction zone model imaged by Rondenay *et al.* [2008], with a Moho undulation around 10 km and a two-layer subducted slab: a slower subducted oceanic crust layer of  $-6.0\%$  variation in  $\rho$ ,  $V_p$ , and  $V_s$ , atop a fast subducted lithospheric mantle layer of  $4.0\%$  perturbation in  $\rho$ ,  $V_p$ , and  $V_s$ . Figure 2b is a simplified version of Figure 2a without slab anomalies. Figure 2c is a 1-D crust-mantle model with a flat Moho at 30 km. Inverted triangles indicate the 20 seismic array stations with equal spacing of 10 km deployed along the  $x$  axis along  $y = 100 \text{ km}$  at the surface. (d–l) Seismic profiles computed by the 3-D SEM-FK hybrid method for a  $P$  wave incidence (incident angle  $\theta = 15^\circ$  and azimuth angle  $\phi = 45^\circ$ ) recorded by the seismic array for the two-layer subducted slab model (Figures 2d–2f), the Moho variation-only model (Figures 2g–2i), and the 1-D crust-mantle model (Figures 2j–2l), showing the radial ( $U_r$ ), transverse ( $U_t$ ), and vertical ( $U_z$ ) component displacement seismograms aligned on the first  $P_p$  arrival. The circled numbers indicate the predicted arrivals of the seven Moho-related phases labeled in Figure 1b based on the 1-D model in Figure 2c.

and vertical synthetic displacement seismograms for these three models and align them on the first  $P_p$  arrivals (Figures 2d–2l). It can be observed that incident and scattered energy are mainly confined to the vertical plane parallel to the propagation direction of the incoming plane  $P$  waves. Only minor scattered waves appear in the transverse direction due to the oblique incidence onto the 2-D models (Figures 2e and 2h) while none appears for the 1-D model (Figure 2k). Moho variations of these three models can be estimated from the radial and vertical seismic profiles by analyzing converted seismic phases such as  $P_s$  (Figures 2d, 2g, and 2j) and reflected phases such as  $PpPmp$  (Figures 2f, 2i, and 2l). Seismograms for the Moho+slab model (Figures 2d–2f) are similar to those for the Moho-only model (Figures 2g–2i), except some notable differences in the later arrivals of the radial component (Figures 2d and 2g). This implies that Moho

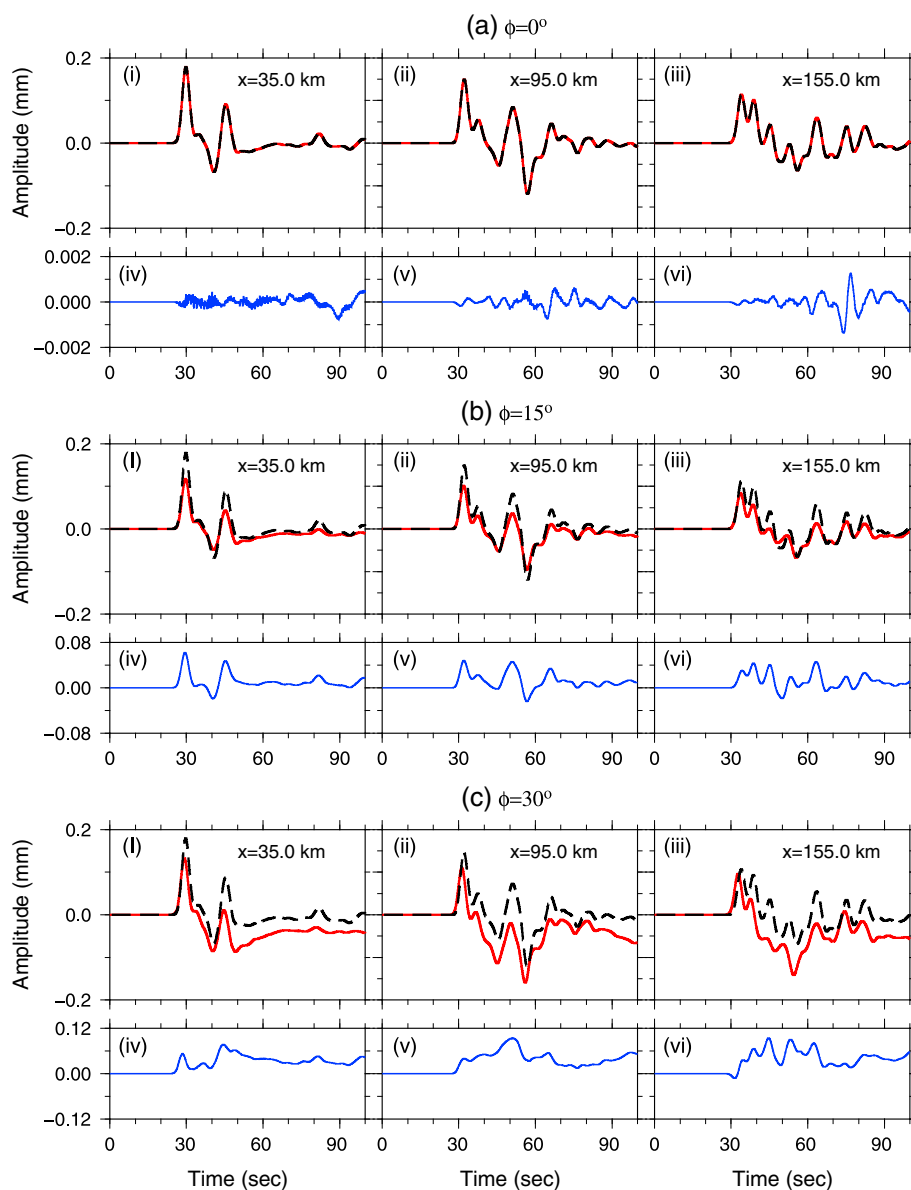


**Figure 3.** Synthetic radial displacement seismograms generated by the 2-D (dashed curves) and 3-D (red curves) SEM-FK hybrid methods as well as their difference (blue curves) recorded at three stations located at  $x = 35, 95$ , and  $155$  km at the surface for the Alaska subduction zone model of Figure 2a, for plane  $P$  waves with incident angle of  $\theta = 15^\circ$  and azimuth angles of (a)  $\phi = 0^\circ$ , (b)  $\phi = 15^\circ$ , and (c)  $\phi = 30^\circ$ . The cut-off frequency of the source is  $f_0 = 0.5$  Hz.

discontinuities have a dominant (first-order) effect on the teleseismic scattered waves considering the large velocity contrasts ( $\sim 30\%$ ) between the crust and the mantle (Table 1). Nonetheless, seismic scattered/coda waves following the direct arrivals are crucial in mapping both the complex slab structure and the Moho topography. For example, based on a 2-D SEM-FK hybrid method and adjoint tomographic techniques, *Tong et al.* [2014] recovered the 2-D structure of Figure 2a from a simple 1-D initial model (Figure 2c) through the waveform inversion of teleseismic scattered waves [see *Tong et al.*, 2014, Figure 17].

We also examine the validity of 2-D numerical modeling of oblique plane wave incidence for a medium varying only in two dimensions, and invariant in the third dimension (also known as 2.5-D), as generating 3-D wavefield for 2.5-D models based on 2-D numerical techniques is widely used to achieve computational efficiency [e.g., *Takenaka and Kennett*, 1996; *Roecker et al.*, 2010]. With the full 3-D SEM-FK method, we test the accuracy of 2-D SEM-FK modeling for 2.5-D models such as the Alaska subduction zone model in Figure 2a. We calculate synthetic seismograms for three plane  $P$  waves with different azimuth angles of



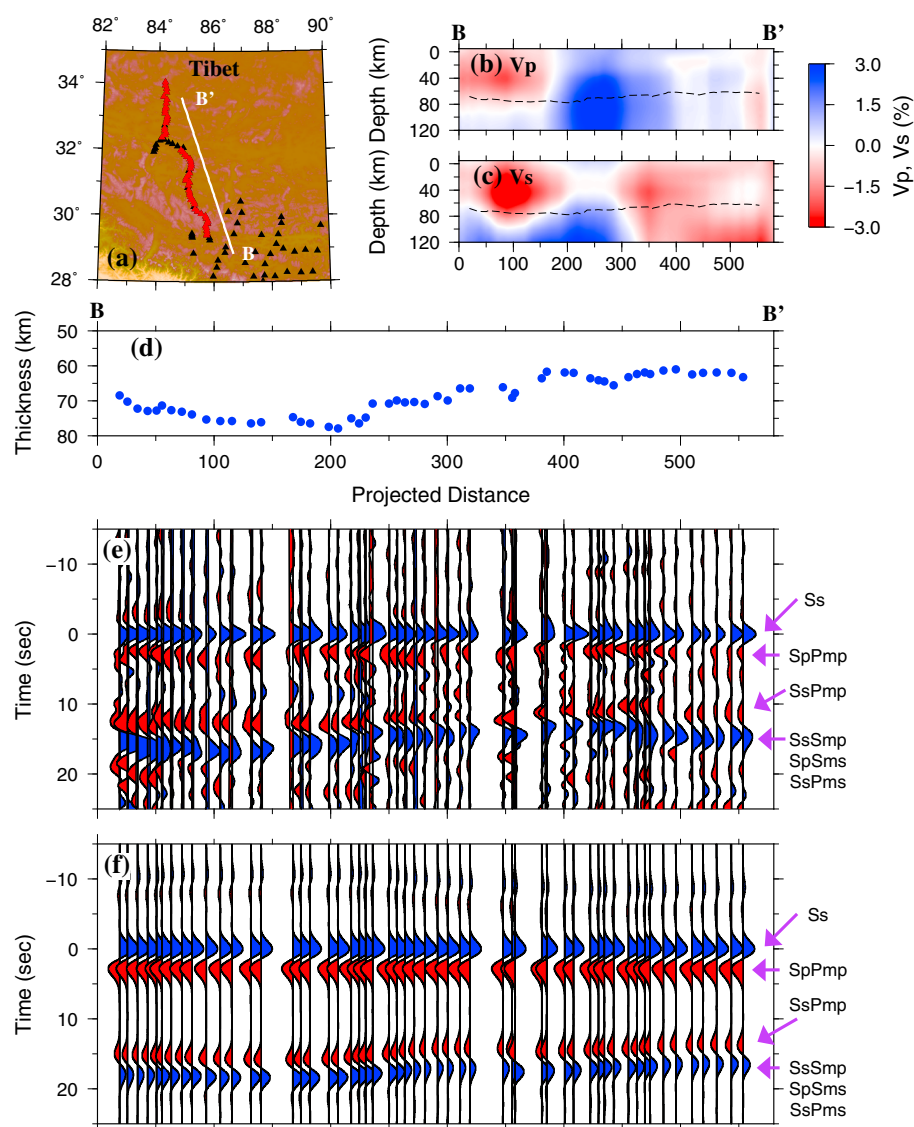


**Figure 4.** (a) Geographic distributions of Hi-CLIMB stations (triangles) previously deployed in central Tibet. Red triangles indicate stations used to generate the observed and synthetic RF profiles in Figures 4e and 4f. BB' is the profile along which the crust thickness was estimated by Tseng et al. [2009]. (b)  $V_p$  and (c)  $V_s$  perturbations along Profile BB' mapped by Hung et al. [2011] superimposed onto the estimated Moho. (d) Estimated crust thickness (blue dots) based on  $T_{SsPmp} - T_{Ss}$  by Tseng et al. [2009]. (e) Observed SV wave seismic reflection profile (vertical-component velocity) for a 2005 earthquake occurred at 5.32°N, 123.34°E, and a depth of 522 km. Various scattered/converted phases, including SsPmp, are indicated by purple arrows. (f) Corresponding synthetic SV wave seismic profile computed by the 3-D SEM-FK hybrid method based on a local crustal model that incorporates CRUST1.0, the estimated Moho profile, and the 3-D  $V_p$  and  $V_s$  variations. All seismograms in Figures 4e and 4f are aligned on the Ss phase.

$\phi = 0^\circ$ ,  $\phi = 15^\circ$ , and  $\phi = 30^\circ$  and the same incident angle of  $\theta = 15^\circ$  based on the 2-D and the 3-D SEM-FK hybrid methods separately (Figure 3), with those computed based on the 3-D SEM-FK hybrid method serving as ground truth to assess the validity of the 2-D SEM-FK. As expected, waveforms match very well (with less than 0.5% difference) for  $\phi = 0^\circ$  in-plane P waves as the 2.5-D model degenerates to 2-D model for this case (Figure 3a). Seismic phases match reasonably well for the case of  $\phi = 15^\circ$  (Figure 3b), although the 2-D SEM-FK seems to overestimate the amplitudes. For oblique incident waves with azimuth angle of  $\phi = 30^\circ$ , both amplitudes and waveforms differ quite significantly (Figure 3c), and small phase shifts can be observed for some phases. These observations suggest that 2-D SEM-FK hybrid method can be used to simulate oblique plane wave propagation in 2.5-D models for the purpose of computational efficiency only if the azimuth angle is reasonably small and only phase information is used in seismic array analysis. However,

when the azimuth angle of incident waves is relatively large for the 2.5-D model, or when the model varies significantly in 3-D, it becomes necessary to resort to 3-D SEM-FK calculations.

### 3.3. Central Tibet Crustal Model

Tibet is formed by the collision of the Indian and Eurasia plate (Figure 4a) [e.g., Kind *et al.*, 2002; Nunn *et al.*, 2014]. It has an average elevation of more than 5 km and crustal thickness of about 80 km, and the mechanisms for its deformation and high topography remain controversial [e.g., Owens and Zandt, 1997; Aitchison *et al.*, 2007; Nunn *et al.*, 2014]. A densely spaced broadband seismic array Hi-CLIMB was previously deployed in central Tibet to address some of these tectonic questions [e.g., Chen and Tseng, 2007; Chen *et al.*, 2010]. Through these high-quality data, Hung *et al.* [2010] investigated 3-D *P* and *S* wave velocity variations beneath central Tibet (Figures 4b and 4c) through multiscale finite-frequency tomography, while Tseng *et al.* [2009] reported a northward thinning of the Tibetan crust (Figure 4d or 2c in the original article) with the surface-converted and Moho-reflected seismic phase *SsPmp* from an *SV* wave receiver function profile computed for a 2005 earthquake occurred at (5.32°N, 123.34°E) and a depth of 522 km (Figure 4e or 2b in Tseng *et al.* [2009]).

In this study, we model this *SV* receiver function profile with the 3-D SEM-FK hybrid method to validate the velocity model inverted by Hung *et al.* [2010] and the Moho variations observed by Tseng *et al.* [2009]. We build a central Tibet layered crustal model that consists of the upper, middle, and lower crust, as well as the uppermost mantle layer based on the CRUST1.0 model [Laske *et al.*, 2013]. In addition, the Moho geometry along Profile BB' recovered by Tseng *et al.* [2009] and the tomographic models resolved by Hung *et al.* [2011] as 3-D variations (Figures 4b–4d) are also incorporated. We simulate a plane *SV* wave incidence with an incidence angle of  $\theta = 32.5^\circ$  determined by  $\tau$ -*p* method [Crotwell *et al.*, 1999] based on the average epicentral distance of this 2005 earthquake to the Hi-CLIMB array. The cut-off frequency of the source-time function is chosen to be  $f_0 = 0.4$  Hz based on the frequency content of the observed *SV* receiver function profile [Tseng *et al.*, 2009].

Figure 4f shows the synthetic vertical-component *SV*-receiver profile computed by the 3-D SEM-FK hybrid method. Compared to the observed profile (Figure 4e), the polarity and amplitudes of the reflected/converted phases of synthetic seismograms are generally consistent with those of the data. Four groups of distinct seismic phases, including *Ss*, *SpPmp*, *SsPmp*, and *SsSmp* (*SsPms*, *SpSms*), can be observed in both the data and synthetics. The earlier arrivals of the synthetic *SsPmp* phase toward the northern section of BB' profile clearly reflect the northward thinning of the input Moho. We also notice that the synthetic *SsPmp* phases have on average a time delay of about 2 s compared to the data, an indication that the *S* velocities of the crust may have been underestimated in the numerical model. Different from the synthetics (Figure 4f) in which only clear and distinct converted/scattered phases are seen on the profile, numerous small-amplitude scattered waves are observable between *SpPmp* and *SsPmp* and following the *SsSmp* waves in the observed profile (Figure 4e). These scattered phases suggest a much more complex central Tibet crust than the present numerical model, and the further improvement of the central Tibet crustal model based on teleseismic seismic scattered/coda waves by combining 3-D SEM-FK forward modeling technique with waveform-based adjoint tomography [Tong *et al.*, 2014] remains to be our future work.

## 4. Discussions and Future Work

From the stacking of receiver functions to the stacking of singly scattered wavefields along hyperbolae, and to the methods that invoke inversion/backprojection of scattered teleseismic wavefields, teleseismic array imaging techniques treat the scattering problems gradually in a more general and complex fashion [Rondenay, 2009]. Accurate modeling of the propagation of teleseismic waves in local 2-D/3-D heterogeneous structures will thus eventually become a necessary ingredient for the further development of seismic array analysis.

Although full numerical simulations of teleseismic waves from source to seismic stations at periods relevant to regional scattering imaging are still computationally prohibitive, the developed 3-D SEM-FK hybrid method that interfaces incident semianalytical FK solutions for 1-D background media with accurate SEM simulations of plane wave propagation in 3-D local media makes it feasible to model teleseismic body waves at very high frequencies ( $\sim 1$  s) with current standard computational resources. Complex wave phenomena associated with interactions between teleseismic plane waves and local heterogeneities are accurately captured by this hybrid method, as we have shown for both the subduction zone model and the central



Tibet crustal model. Hence, the accurate modeling of local media by SEM-FK hybrid methods also offers an independent benchmarking methodology that may be used to validate Moho profiles or regional models generated by the traditional scattering imaging techniques. In the near future, we plan to incorporate the 3-D SEM-FK hybrid method into the popular open-source community software package SPECFEM3D that simulates regional seismic wave propagation (<http://geodynamics.org/cig/software/specfem3d>) and allow researchers to produce synthetic receiver function profiles and validate Moho variations as well as structural models mapped based on their own imaging techniques from scattered/coda waves. By definition of our one-way coupling strategy, one should keep in mind that scattered waves generated by 3-D heterogeneities superimposed to the 1-D background model cannot be further modeled by this hybrid method when they travel out of the SEM domain and are reflected back into that SEM domain off 1-D interfaces located inside the F-K domain. This is by construction the main limitation of the approach that we have chosen. For a more complete but also more involved, fully coupled strategy one can refer for instance to Capdeville *et al.* [2003a, 2003b].

The 3-D SEM-FK hybrid method developed in this study also provides an important tool for the further development of high-resolution teleseismic array analysis. First, the flexibility of the SEM in treating complex geometry and heterogeneity in local computational domains eliminates nearly all restrictions on the background media for forward modeling. Second, a realistic 2-D/3-D heterogeneous background model and undulations of internal discontinuities will provide better estimates of the scattered wavefields compared to the assumption of a 1-D background model in RF analysis. Furthermore, using a 3-D SEM-FK implementation enables accurate modeling of teleseismic plane waves incident from all azimuth and thus increases the illumination beneath the array [Burdick *et al.*, 2014]. All these advantages of the 3-D SEM-FK hybrid method, together with the ability of adjoint tomography in exploring the full waveform information of array data, should enable the community to obtain high-quality crustal and upper mantle images with increased resolution based on realistic seismic array recordings.

#### Acknowledgments

This research was supported by the G8 Research Councils Initiative on Multilateral Research Grant and the Discovery Grants of the Natural Sciences and Engineering Research Council of Canada (NSERC), by the French ANR under grant 2010-G8EX-002-03, by the European "Mont-Blanc: European scalable and power efficient HPC platform based on low-power embedded technology" 288777 project of call FP7-ICT-2011-7, and by the Simone and Cino Del Duca Foundation of the French Academy of Sciences. Computations for this study were performed on hardwares acquired through the combined funding of Canada Foundation for Innovation (CFI), Ontario Research Fund (ORF) and University of Toronto Startup Fund, and partly hosted by the SciNet HPC Consortium. We thank M. Wyssession, Y. Capdeville, and another anonymous reviewer for providing constructive comments and suggestions that improved the manuscript.

Michael Wyssession thanks Yann Capdeville and Li Zhao for their assistance in evaluating this paper.

#### References

- Aitchison, J., J. Ali, and A. Davis (2007), When and where did India and Asia collide?, *J. Geophys. Res.*, *112*, B05423, doi:10.1029/2006JB004706.
- Aki, K., and P. G. Richards (2002), *Quantitative Seismology: Theory and Methods*, 2nd ed., Univ. Science Books, Sausalito, Calif.
- Bielak, J., and P. Christiano (1984), On the effective seismic input for non-linear soil-structure interaction systems, *Earthquake Engng. Struct. Dyn.*, *12*, 107–119.
- Bostock, M. G., S. Rondenay, and J. Shragge (2001), Multiparameter two-dimensional inversion of scattered teleseismic body waves 1. Theory for oblique incidence, *J. Geophys. Res.*, *106*(12), 30,771–30,782.
- Burdick, S., M. V. de Hoop, S. Wang, and R. D. V. D. Hilst (2014), Reverse-time migration-based reflection tomography using teleseismic free surface multiples, *Geophys. J. Int.*, *196*, 996–1017, doi:10.1093/gji/ggt428.
- Cao, Q., P. Wang, R. van der Hilst, M. de Hoop, and S.-H. Shim (2010), Imaging the upper mantle transition zone with a generalized Radon transform of SS precursors, *Phys. Earth Planet. Inter.*, *180*(1–2), 80–91, doi:10.1016/j.pepi.2010.02.006.
- Capdeville, Y., E. Chaljub, J. P. Vilotte, and J. P. Montagner (2003a), Coupling the spectral element method with a modal solution for elastic wave propagation in global Earth models, *Geophys. J. Int.*, *152*, 34–67.
- Capdeville, Y., B. Romanowicz, and A. To (2003b), Coupling spectral elements and modes in a spherical Earth: An extension to the 'sandwich' case, *Geophys. J. Int.*, *154*, 44–57.
- Chen, L., L. Wen, and T. Zheng (2005), A wave equation migration method for receiver function imaging: 2. Application to the Japan subduction zone, *J. Geophys. Res.*, *110*, B11310, doi:10.1029/2005JB003666.
- Chen, W.-P., and T.-L. Tseng (2007), Small 660-km seismic discontinuity beneath Tibet implies resting ground for detached lithosphere, *J. Geophys. Res.*, *112*, B05309, doi:10.1029/2006JB004607.
- Chen, W.-P., M. Martin, T.-L. Tseng, R. Nowack, S.-H. Hung, and B.-S. Huang (2010), Shear-wave birefringence and current configuration of converging lithosphere under Tibet, *Earth Planet. Sci. Lett.*, *295*(1–2), 297–304.
- Clayton, R., and B. Engquist (1977), Absorbing boundary conditions for acoustic and elastic wave equations, *Bull. Seismol. Soc. Am.*, *67*, 1529–1540.
- Crotwell, H. P., T. J. Owens, and J. Ritsema (1999), The TauP toolkit: Flexible seismic travel-time and ray-path utilities, *Seismol. Res. Lett.*, *70*, 154–160.
- Frederiksen, A. W., and J. Revenaugh (2004), Lithospheric imaging via teleseismic scattering tomography, *Geophys. J. Int.*, *159*, 978–990.
- Haskell, N. B. (1953), The dispersion of surface waves on multilayered media, *Bull. Seismol. Soc. Am.*, *43*(1), 17–34.
- Hung, S.-H., W.-P. Chen, L.-Y. Chiao, and T.-L. Tseng (2010), First multi-scale, finite-frequency tomography illuminates 3-D anatomy of the Tibetan plateau, *Geophys. Res. Lett.*, *37*, L06304, doi:10.1029/2009GL041875.
- Hung, S.-H., W.-P. Chen, and L.-Y. Chiao (2011), A data-adaptive, multiscale approach of finite-frequency, traveltimes tomography with special reference to *P* and *S* wave data from central Tibet, *J. Geophys. Res.*, *116*, B06307, doi:10.1029/2010JB008190.
- Kind, R., *et al.* (2002), Seismic images of crust and upper mantle beneath Tibet: Evidence for Eurasian plate subduction, *Science*, *298*, 1219–1221.
- Kind, R., X. Yuan, and P. Kumar (2012), Seismic receiver functions and the lithosphere-asthenosphere boundary, *Tectonophysics*, *536–537*, 25–43, doi:10.1016/j.tecto.2012.03.005.
- Komatitsch, D., and J. Tromp (1999), Introduction to the spectral element method for three-dimensional seismic wave propagation, *Geophys. J. Int.*, *139*, 806–822.

- Komatitsch, D., Q. Liu, J. Tromp, M. P. Suss, C. Stidham, and J. H. Shaw (2004), Simulations of ground motion in the Los Angeles Basin based upon the spectral-element method, *Bull. Seismol. Soc. Am.*, *94*, 187–206.
- Komatitsch, D., P. Vinnik, and S. Chevrot (2010), SHdiff-SVdiff splitting in an isotropic Earth, *J. Geophys. Res.*, *115*, B07312, doi:10.1029/2009JB006795.
- Langston, C. A. (1977), Corvallis, Oregon, crustal and upper mantle receiver structure from teleseismic *P* and *S* waves, *Bull. Seismol. Soc. Am.*, *67*, 713–724.
- Laske, G., G. Masters, Z. Ma, and M. Pasyanos (2013), Update on CRUST1.0-A 1-degree global model of Earth's crust, paper presented at EGU General Assembly, EGU2013-2658, Vienna, Austria, 7–12 April.
- Liu, Q., and Y. J. Gu (2012), Seismic imaging: From classical to adjoint tomography, *Tectonophysics*, *566–567*, 31–66, doi:10.1016/j.tecto.2012.07.006.
- Monteiller, V., S. Chevrot, D. Komatitsch, and N. Fuji (2013), A hybrid method to compute short period synthetic seismograms of teleseismic body waves in a 3-D regional model, *Geophys. J. Int.*, *192*, 230–247.
- Nunn, C., S. Roecker, F. Tilmann, K. Priestley, R. Heyburn, E. Sandvol, J. Ni, Y. Chen, and W. Zhao (2014), Imaging the lithosphere beneath NE Tibet: Teleseismic *P* and *S* body wave tomography incorporating surface wave starting model, *Geophys. J. Int.*, *196*, 1724–1741.
- Owens, T., and G. Zandt (1997), Implications of crustal property variations for models of Tibetan plateau evolution, *Nature*, *387*, 37–43.
- Pageot, D., S. Operto, M. Vallee, R. Brossier, and J. Virieux (2013), A parametric analysis of two-dimensional elastic full waveform inversion of teleseismic data for lithospheric imaging, *Geophys. J. Int.*, *193*, 1479–1505.
- Revenaugh, J. (1995), A scattered-wave image of subduction beneath the Transverse Ranges, *Science*, *268*, 1888–1892.
- Roecker, S., B. Baker, and J. McLaughlin (2010), A finite-difference algorithm for full waveform teleseismic tomography, *Geophys. J. Int.*, *181*, 1017–1040.
- Rondenay, S. (2009), Upper mantle imaging with array recordings of converted and scattered teleseismic waves, *Surv. Geophys.*, *30*, 377–405, doi:10.1007/s10712-009-9071-5.
- Rondenay, S., G. A. Abers, and P. E. van Keken (2008), Seismic imaging of subduction zone metamorphism, *Geology*, *36*, 275–278.
- Shang, X., M. V. de Hoop, and D. van der Hilst (2012), Beyond receiver functions: Passive source reverse time migration and inverse scattering of converted waves, *Geophys. Res. Lett.*, *39*, L15308, doi:10.1029/2012GL052289.
- Shang, X., S.-H. Shim, M. de Hoop, and R. van der Hilst (2014), Multiple seismic reflectors in Earth's lowermost mantle, *Proc. Nat. Acad. Sci.*, *111*, 2442–2446, doi:10.1073/pnas.1312647111.
- Sheehan, A. F., P. M. Shearer, H. J. Gilbert, and K. G. Dueker (2000), Seismic migration processing of P-SV converted phases for mantle discontinuity structure beneath the Snake River Plain, western United States, *J. Geophys. Res.*, *105*(B8), 19,055–19,065.
- Shragge, J., B. Artman, and C. Wilson (2006), Teleseismic shot-profile migration, *Geophysics*, *71*(4), SI221–SI229, doi:10.1190/1.2208263.
- Takenaka, H., and B. L. Kennett (1996), A 2.5-D time-domain elastodynamic equation for plane-wave incidence, *Geophys. J. Int.*, *125*, 5–9.
- Takeuchi, H., and M. Saito (1972), Seismic surface waves, in *Methods in Computational Physics*, vol. 11, edited by B. A. Bolt, pp. 217–295, Academic Press, New York.
- Tape, C., Q. Liu, A. Maggi, and J. Tromp (2009), Adjoint tomography of the Southern California crust, *Science*, *325*, 988–992.
- Thomson, W. (1950), Transmission of elastic waves through a stratified solid medium, *J. Appl. Phys.*, *21*, 89–93.
- Tong, P., C.-W. Chen, D. Komatitsch, P. Basini, and Q. Liu (2014), High-resolution seismic array imaging based on an SEM-FK hybrid method, *Geophys. J. Int.*, *197*, 369–395.
- Tromp, J., C. Tape, and Q. Liu (2005), Seismic tomography, adjoint methods, time reversal and banana-doughnut kernels, *Geophys. J. Int.*, *160*, 195–216.
- Tromp, J., J. Komatitsch, and Q. Liu (2008), Spectral-element and adjoint methods in seismology, *Comm. Comput. Phys.*, *3*, 1–32.
- Tseng, T.-L., W.-P. Chen, and R. L. Nowack (2009), Northward thinning of Tibetan crust revealed by virtual seismic profiles, *Geophys. Res. Lett.*, *36*, L24304, doi:10.1029/2009GL040457.
- Yan, Z., and R. W. Clayton (2007), Regional mapping of the crustal structure in southern California from receiver functions, *J. Geophys. Res.*, *112*, B05311, doi:10.1029/2006JB004622.
- Zhu, L., and L. A. Rivera (2002), A note on the dynamic and static displacements from a point source in multilayered media, *Geophys. J. Int.*, *148*, 619–627.